Impacts of Varying Model Physics on Simulated Structures in RCE Cloud Systems

Andrew T. Lesage* and Steven K. Krueger

Department of Atmospheric Sciences, University of Utah, Salt Lake City, Utah

**Corresponding author address:* Andrew T. Lesage, Department of Atmospheric Sciences, 135 S 1460 E, Rm 819, Salt Lake City, Utah 84112-0110.

E-mail: andy.lesage@utah.edu

ABSTRACT

Put in an abstract.

1. Introduction

Turbulence parameterization methodology has had an important role in model handling of clouds. Early versions of turbulence parameterizations used a diagnostic equation to solve for K, the eddy viscosity (Pielke 1974). Other methods sought a prognostic turbulent kinetic energy (TKE) equation though even second-moment schemes at times had difficulty with vertical transport of TKE (Yamada and Mellor 1975). Third-moment turbulent closure schemes have been used to better capture TKE in the boundary layer and in-cloud (Krueger 1988).

2. Model Background

The System for Atmospheric Modeling (SAM) is used throughout this research as both the Large-Eddy Simulation (LES) model for 100 m grid spacing runs and as a Cloud-Resolving Model (CRM), and is detailed in Khairoutdinov and Randall (2003). SAM uses anelastic equations of motion in the dynamical core integrated with a third-order Adams-Bashforth scheme. Variables are staggered on an Arakawa C grid. The advection is handled with a three-dimensional positive definite monotonic scheme (Smolarkiewicz and Grabowski 1990). SAM prognoses the thermodynamical variables liquid water/ice moist static energy, total non-precipitating water, and total precipitating water. The model does not allow for supersaturation of water vapor, with cloud condensate diagnosed using an ”all-or-nothing” approach.

Radiation in SAM is handled with either the Community Atmospheric Model (CAM) (Collins and Coauthors 2004) or the Rapid Radiative Transfer Model (RRTM) (Mlawer et al. 1997) schemes from the National Center for Atmospheric Research (NCAR) Community Climate System Model (CCSM). Microphysics uses either the original SAM single-moment microphysics or the Morrison double-moment microphysics (Morrison et al. 2005).

The model has periodic boundary conditions and a simple mixed-layer ocean. The Monin-Obukhov similarity theory is used for the surface fluxes. SAM has incorporated ISCCP, MODIS, and MISR cloud simulators with ISCCP simulator results used in this study (Klein and Jakob 1999).

For the turbulence closure scheme SAM comes with two options, a 1.5-order closure using a prognostic equation for the subgrid-scale turbulent kinetic energy (SGS-TKE) (Khairoutdinov and Kogan 1999), and a simple Smagorinsky closure (Khairoutdinov and Randall 2003). The former is used throughout this study and will be referred to as NOSHOC.

A third closure scheme was added called Simplified Higher-Order Closure (SHOC) and is detailed in Bogenschutz and Krueger (2013). Similar to the NOSHOC method, SHOC also prognoses SGS-TKE. An assumed joint PDF is used to diagnose SGS condensation and SGS buoyancy flux (Golaz et al. 2002a,b). The joint PDF is based on vertical velocity, liquid water potential temperature, and total water mixing ratio. Double Gaussian PDFs have been shown to fit cloud layers better than alternatives tested (Bogenschutz et al. 2010).

NOSHOC does not diagnose SGS condensation and SGS buoyancy flux is diagnosed from the moist Brunt-Vaisala frequency. Instead, SHOC uses the diagnostic second-moment closure of Redelsperger and Sommeria (1986) and the diagnostic closure for the third moment of vertical velocity from Canuto et al. (2001).

A key difference between NOSHOC and SHOC is in the handling of the length scale. In NOSHOC, the length scale is proportional to dz. Bogenschutz and Krueger (2013) note that having a length scale set to the vertical grid spacing is appropriate for high resolution simulations where the grid size is in the inertial subrange. In SHOC, the turbulence length scale is instead related to SGS-TKE and eddy length scales which have been shown to be effective for the convective boundary layer (Teixeira and Cheinet 2004). Eddy diffusion schemes have been shown to perform well when the SGS-TKE profile can be predicted (Cheng et al. 2010).

3. Model Runs

Radiative convective equilibrium (RCE) modeling provides a simple proxy for the Earth's climate.

Over 40 model runs have been performed to evaluate cloud and radiative property dependencies on a broad variety of cloud-resolving model (CRM) configurations. Variations in the model configurations include SST, horizontal grid size, microphysics scheme, and turbulence closure scheme. SSTs selected were 301 K and 305 K. Grid sizes used were 0.5, 1, 2, 4, 8, and 16 km. Runs with 0.5 km grid spacing were performed by Marat Khairoutdinov. Microphysics schemes were SAM single-moment microphysics or the M2005 double-moment microphysics (Morrison et al. 2005). Turbulence closure schemes used were standard SAM (NOSHOC) or SAM-SHOC. Runs performed were 50 day simulations.

Runs were first performed on a 256x256 km grid with 84 vertical levels. However, many SAM-SHOC runs experienced self-aggregation and had to be rerun with a 128x128 or 64x64 km grid. Self-aggregation has been shown to occur in RCE simulations as a result of cold pools when domain sizes are sufficiently large (Jeevanjee and Romps 2013). When RCE simulations are not self-aggregating they have been shown to be qualitatively similar across a large range of GCM domain sizes (Silvers et al. 2016). The table of non-aggregating model simulations performed is shown in (Table 1).

By having simulations at different SSTs the temperature dependence of cloud and radiative properties can be determined. Additionally, climate feedbacks can be calculated using radiative kernels (Soden et al. 2008). Eight additional 1 km runs were performed for each combination of

SST, microphysics scheme, and turbulence closure scheme on a 64km domain. The radiative kernels generated from ERA Interim over 2000-2010 (Zhou et al. 2013) were selected over CFMIP1 climate model derived kernels (Zelinka et al. 2012a,b) due to a closer match with SAM statistics file results.

4. Results

From the RCE simulations, dependencies on microphysics, turbulence parameterization scheme, grid spacing, and SST were evaluated. All results detailed in this section are 25-day averages of days 26-50 in model run simulations.

Cloud water path (CWP) and ice water path (IWP) values are presented in Figure 1. There is a large difference in CWP and IWP depending on the microphysics scheme selected with higher CWP and much lower IWP in the double-moment runs. SHOC runs with single-moment microphysics have lower CWP and IWP than the NOSHOC equivalents. Altering the grid spacing results in some phase differences with CWP increasing and IWP decreasing as grid spacing increases, with the increases in CWP much larger in magnitude than the decreases in IWP. The lower SST runs for SHOC had significantly lower CWP than the warmer SST SHOC run and the NOSHOC runs at either SST. These 301 K SHOC runs had very little grid size dependence on CWP.

ISCCP simulated high and low cloud fractions are shown in Figure 2. Simulated high cloud fractions are higher for double-moment runs than single-moment runs. Grid size and SST dependencies are very similar for high cloud fraction compared to ice water path, and low cloud fraction compared to cloud water path. SHOC single-moment runs show a higher high cloud fraction than the NOSHOC runs despite the ice water path being higher for NOSHOC runs.

Cloud radiative effects are shown in Figure 3. Longwave (LW) cloud radiative effect is similar to high cloud fraction while the negative of shortwave (SW) cloud radiative effect is similar to low cloud fraction with the exception of a double-moment SHOC vs NOSHOC gap in LW cloud radiative effect which does not show up in high cloud fraction (Figure 3a-d). The SW cloud radiative effect has a larger influence on the net cloud radiative effect (Figure 3e-f). At large grid sizes all runs except 301 K SHOC runs have large negative value cloud radiative effects. For single-moment NOSHOC runs at the lowest grid sizes (0.5 km and 1 km) net cloud radiative effect is negative; however, for single-moment SHOC runs and all double-moment runs, the average net cloud radiative effect is positive for 1 km runs.

Cloud fraction profiles as a function of temperature are shown in Figure 4. In all cases, low-level cloud fraction decreased as horizontal grid resolution increased. Upper-level cloud top temperature was similar for all runs regardless of SST (a,b,c,d vs e,f,g,h). Upper-level cloud fractions were slightly higher in SHOC runs than their NOSHOC equivalents (c,d,g,h vs a,b,e,f) and for double-moment runs than their single-moment equivalents (b,d,f,h vs a,c,e,g). For NOSHOC runs, lower resolution runs had cooler maximum cloud fraction level temperatures than the higher resolution runs. Lower resolution runs had higher max cloud fractions in all NOSHOC cases. Higher resolution single-moment runs for both SHOC and NOSHOC had a small increase in cloud fraction around 190 K.

ISCCP simulations allowed for cloud histograms separated into 7 pressure bins and 7 optical thickness bins. A set of these results was made for all 8 (varying in SST, microphysics, and turbulence parameterization scheme) 1 km runs. The cloud fraction histograms were multiplied by the ERA interim LW and SW cloud forcing kernels from Zhou et al. (2013) to make histograms of net, LW, and -SW cloud forcing. Results for the NOSHOC 1M 301 K run are shown in Figure 5. The primary cloud type is upper level cirrus in the top left corner of Figure 5a which results in the largest LW and -SW cloud forcings to be in the two lower pressure levels. The net cloud forcing from sea surface temperature is slightly negative in the majority of bins with the exception of upper level cirrus bins which have a positive net cloud forcing.

Average cloud feedbacks could be calculated from pairs of histograms differing in SST (Table 2). The magnitude of the LW and SW cloud feedback was much higher for SHOC runs than NOSHOC runs. For single-moment NOSHOC runs LW and SW feedbacks were both positive resulting in a net cloud feedback of 0.53 $Wm^{-2}K^{-1}$. Double-moment NOSHOC runs resulted in a negative LW cloud feedback and a near zero net cloud feedback. LW feedbacks were positive for SHOC runs while SW feedbacks were negative for SHOC runs with roughly a 50% higher magnitude in SW feedback yielding a net cloud feedback of -0.55 and -0.50 $Wm^{-2}K^{-1}$ for single and double-moment SHOC respectively.

Vertical layer profiles of cloud fraction and cloud feedbacks are shown in Figure 6. For all microphysics and turbulence closure scheme configurations the layer cloud fraction increases with warmer SST at the highest layer and decreases at the second highest layer. This change is primarily a result of the temperature level of cloud tops remaining roughly the same, as shown in Figure 4, while the height of the same temperature level increases with SST. The cloud fraction changes are quite small, on the order of 1%. In the lower to middle troposphere SHOC runs have a very slightly positive cloud fraction feedback while NOSHOC runs have a very slightly negative cloud fraction feedback. Net cloud feedback is positive for NOSHOC runs except for the highest layer and second lowest layer. For SHOC runs net cloud feedback is negative in the lower to middle troposphere and positive for the two highest layers. The net cloud feedback values are of lower magnitude at the highest levels than those of LW and SW cloud feedback, a result of the LW and SW feedbacks largely canceling out. Since there is almost no LW cloud feedback in the lower to middle troposphere the SW cloud feedback dominates in that range.

5. Conclusions

Add in conclusions.

Acknowledgments. RCE 0.5 km simulations were run by Marat Khairoutdinov. This research was supported by the Office of Science (BER), U. S. Department of Energy, and by the National Science Foundation Science and Technology Center for Multi-Scale Modeling of Atmospheric Processes, managed by Colorado State University under cooperative agreement No. ATM-0425247.

References

Bogenschutz, P. A., and S. K. Krueger, 2013: A simplified PDF parameterization of subgrid-scale clouds and turbulence for cloud-resolving models. *J. Adv. Model. Earth Syst.*, **5**, 195–211., doi: 10.1002/jame.20018.

Bogenschutz, P. A., S. K. Krueger, and M. Khairoutdinov, 2010: Assumed probability density functions for shallow and deep convection. *J. Adv. Model. Earth Syst.*, **2**, 24 pp., doi:10.3894/JAMES.2010.2.10.

Canuto, V. M., Y. Cheng, and A. Howard, 2001: New third-order moments for the convective boundary layer. *J. Atmos. Sci.*, **58**, 1169–1172., doi:10.1175/1520-0469(2001)058⟨1169:NTOMFT⟩2.0.CO;2.

Cheng, A., K.-M. Xu, and B. Stevens, 2010: Effects of resolution on the simulation of boundary-layer clouds and the partition of kinetic energy to subgrid scales. *J. Adv. Model. Earth Syst.*, **2**, 21 pp., doi:10.3894/JAMES.2010.2.3.

Collins, W. D., and Coauthors, 2004: Description of the NCAR Community Atmospheric Model (CAM 3.0). Tech. rep., NCAR Tech. Note, Note NCAR/TN-464+STR, 226 pp. doi:10.5065/D63N21CH.

Golaz, J. C., V. E. Larson, and W. R. Cotton, 2002a: A PDF-based model for boundary layer clouds. Part I: Method and model description. *J. Atmos. Sci.*, **59**, 3540–3551., doi:10.1175/1520-0469(2002)059⟨3540:APBMFB⟩2.0.CO;2.

Golaz, J. C., V. E. Larson, and W. R. Cotton, 2002b: A PDF-based model for boundary layer clouds. Part II: Model results. *J. Atmos. Sci.*, **59**, 3552–3571., doi:10.1175/1520-0469(2002)059⟨3552:APBMFB⟩2.0.CO;2.

Jeevanjee, N., and D. M. Romps, 2013: Convective self-aggregation, cold pools, and domain size. *Geophys. Res. Lett.*, **40**, 994–998, doi:10.1002/grl.50204.

Khairoutdinov, M., and Y. L. Kogan, 1999: A large-eddy simulation model with explicit microphysics: Validation against aircraft observations of a stratocumulus-topped boundary layer. *J. Atmos. Sci.*, **56**, 2115–2131., doi:10.1175/1520-0469(1999)056⟨2115:ALESMW⟩2.0.CO;2.

Khairoutdinov, M., and D. Randall, 2003: Cloud resolving modeling of the ARM summer 1997 IOP: Model formulations, results, uncertainties, and sensitivities. *J. Atmos. Sci.*, **60**, 607–625., doi:10.1175/1520-0469(2003)060⟨0607:CRMOTA⟩2.0.CO;2.

Klein, S. A., and C. Jakob, 1999: Validation and sensitivities of frontal clouds simulated by ECMWF model. *Mon. Wea. Rev.*, **127**, 2514–2531., doi:10.1175/1520-0493(1999)127⟨2514:VASOFC⟩2.0.CO;2.

Krueger, S. K., 1988: Numerical simulation of tropical cumulus clouds and their interaction with the subcloud layer. *J. Atmos. Sci.*, **45**, 2221–2250., doi:10.1175/1520-0469(1988)045⟨2221:NSOTCC⟩2.0.CO;2.

Mlawer, E. J., S. J. Taubman, P. D. Brown, M. J. Iacono, and S. A. Clough, 1997: Radiative transfer for inhomogeneous atmosphere: RRTM, a validated correlated-*k* model for the longwave. *J. Geophys. Res.*, **102**, 16 663–16 682., doi:10.1029/97JD00237.

Morrison, H., J. A. Curry, and V. I. Khvorostyanov, 2005: A new double-moment microphysics parameterization for application in cloud and climate models. Part I: Description. *J. Atmos. Sci.*, **62**, 1665–1677., doi:10.1175/JAS3446.1.

Pielke, R. A., 1974: A three-dimensional numerical model of the sea breezes over South Florida. *Mon. Wea. Rev.*, **102**, 115–139., doi:10.1175/1520-0493(1974)102⟨0115:ATDNMO⟩2.0.CO;2.

Redelsperger, J. L., and G. Sommeria, 1986: Three-dimensional simulation of a convective storm: Sensitivity studies on subgrid parameterization and spatial resolution. *J. Atmos. Sci.*, **43**, 2619–2635., doi:10.1175/1520-0469(1986)043⟨2619:TDSOAC⟩2.0.CO;2.

Silvers, L. G., B. Stevens, T. Mauritsen, and M. Giorgetta, 2016: Radiative convective equilibrium as a framework for studying the interaction between convection and its large-scale environment. *J. Adv. Model. Earth Syst.*, **8**, 15 pp., doi:10.1002/2016MS000629.

Smolarkiewicz, P. K., and W. W. Grabowski, 1990: The multi-dimensional positive definite advection transport algorithm: Non-oscillatory option. *J. Comput. Phys.*, **86**, 355–375., doi:10.1016/0021-9991(90)90105-A.

Soden, B. J., I. M. Held, R. Colman, K. M. Shell, J. T. Kiehl, and C. A. Shields, 2008: Quantifying climate feedbacks using radiative kernals. *J. Climate*, **21**, 3504–3520., doi:10.1175/2007JCLI2110.1.

Teixeira, J., and S. Cheinet, 2004: A simple mixing length formulation for the eddy-diffusivity parameterization of dry convection. *Bound.-Layer Meteor.*, **110**, 435–453., doi:10.1023/B:BOUN.0000007230.96303.0d.

Yamada, T., and G. Mellor, 1975: A simulation of the Wangara atmospheric boundary layer data. *J. Atmos. Sci.*, **32**, 2309–2329., doi:10.1175/1520-0469(1975)032⟨2309:ASOTWA⟩2.0.CO;2.

Zelinka, M. D., S. A. Klein, and D. L. Hartmann, 2012a: Computing and partitioning cloud feedbacks using cloud property histograms. Part I: Cloud radiative kernels. *J. Climate*, **25**, 3715–3735., doi:10.1175/JCLI-D-11-00248.1.

Zelinka, M. D., S. A. Klein, and D. L. Hartmann, 2012b: Computing and partitioning cloud feedbacks using cloud property histograms. Part II: Attribution to changes in cloud amount, altitude, and optical depth. *J. Climate*, **25**, 3736–3754., doi:10.1175/JCLI-D-11-00249.1.

Zhou, C., M. D. Zelinka, A. E. Dessler, and P. Yang, 2013: An analysis of the short-term cloud feedback using MODIS data. *J. Climate*, **26**, 4803–4815., doi:10.1175/JCLI-D-12-00547.1.

LIST OF TABLES

Table 1. Model simulations performed for the RCE case. 14

Table 2. Radiative kernel-derived cloud feedback values for 1 km RCE simulations computed over last 25-day averages. 15

TABLE 1. Model simulations performed for the RCE case.

RCE Run Setup			Grid Spacing (km)					
SST	Microphys.	Turb.	16	8	4	2	1	0.5
301 K	1M	NOSHOC	256	256	256	256	256	256
		SHOC	128	128	128	128	128	N/A
	2M	NOSHOC	256	256	256	256	256	N/A
		SHOC	128	128	64	64	64	N/A
305 K	1M	NOSHOC	256	256	256	256	256	256
		SHOC	128	128	128	256	256	N/A
	2M	NOSHOC	256	256	256	256	256	N/A
		SHOC	128	128	64	64	64	N/A
			Domain Size (km)					

TABLE 2. Radiative kernel-derived cloud feedback values for 1 km RCE simulations computed over last 25-day averages.

Avg. Cloud Feedback (W m^{-2} K^{-1})	1M NOSHOC	2M NOSHOC	1M SHOC	2M SHOC
LW	0.17	-0.12	1.27	1.01
SW	0.36	0.17	-1.82	-1.51
Net	0.53	0.05	-0.55	-0.50

LIST OF FIGURES

Fig. 1. RCE simulation 25-day averaged values of: a) ice water path for single-moment microphysics runs, b) ice water path for double-moment microphysics runs, c) cloud water path for single-moment microphysics runs, and d) cloud water path for double-moment microphysics runs. Each panel shows runs varying in grid size, SST, and turbulence parameterization scheme. 17

Fig. 2. RCE simulation 25-day averaged values of: a) ISCCP simulated high cloud fraction for single-moment microphysics runs, b) ISCCP simulated high cloud fraction for double-moment microphysics runs, c) ISCCP simulated low cloud fraction for single-moment microphysics runs, and d) ISCCP simulated low cloud fraction for double-moment microphysics runs. Each panel shows runs varying in grid size, SST, and turbulence parameterization scheme. 18

Fig. 3. RCE simulation 25-day averaged values of: a) LW cloud radiative effect for single-moment microphysics runs, b) LW cloud radiative effect for double-moment microphysics runs, c) SW cloud radiative effect for single-moment microphysics runs, d) SW cloud radiative effect for double-moment microphysics runs, e) net cloud radiative effect for single-moment microphysics runs, and f) net cloud radiative effect for double-moment microphysics runs. Each panel shows runs varying in grid size, SST, and turbulence parameterization scheme. . . 19

Fig. 4. RCE simulation 25-day averaged values of cloud fraction as a function of temperature. Panels separate runs based on 301 K SST (a,b,c,d) vs 305 K SST (e,f,g,h), NOSHOC (a,b,e,f) vs SHOC (c,d,g,h), and single-moment (a,c,e,g) vs double-moment (b,d,f,h) microphysics. . . 20

Fig. 5. RCE 25-day averaged 1-km single-moment NOSHOC 301K simulation cloud radiative kernel derived: a) cloud fraction, b) net cloud forcing, c) LW cloud forcing, and d) -1 * SW cloud forcing. Colorbars for a, c, and d are logarithmic. 21

Fig. 6. Vertical profiles of 25-day averaged cloud radiative kernel derived: a) cloud fraction feedback, b) net cloud feedback, c) LW cloud feedback, and d) -1 * SW cloud feedback. Y-axis points are layer means of the pressures in Figure 9. 22

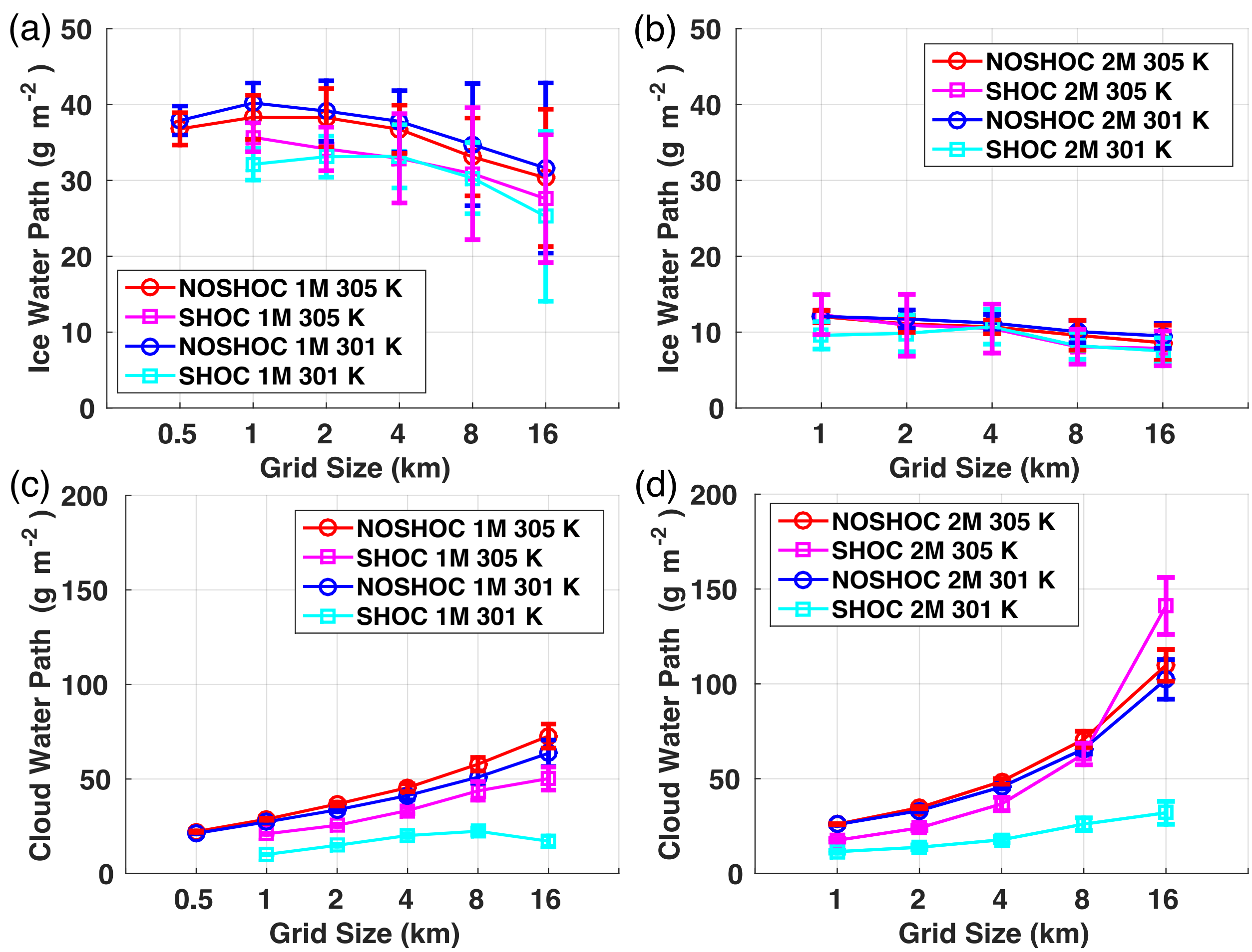

FIG. 1. RCE simulation 25-day averaged values of: a) ice water path for single-moment microphysics runs, b) ice water path for double-moment microphysics runs, c) cloud water path for single-moment microphysics runs, and d) cloud water path for double-moment microphysics runs. Each panel shows runs varying in grid size, SST, and turbulence parameterization scheme.

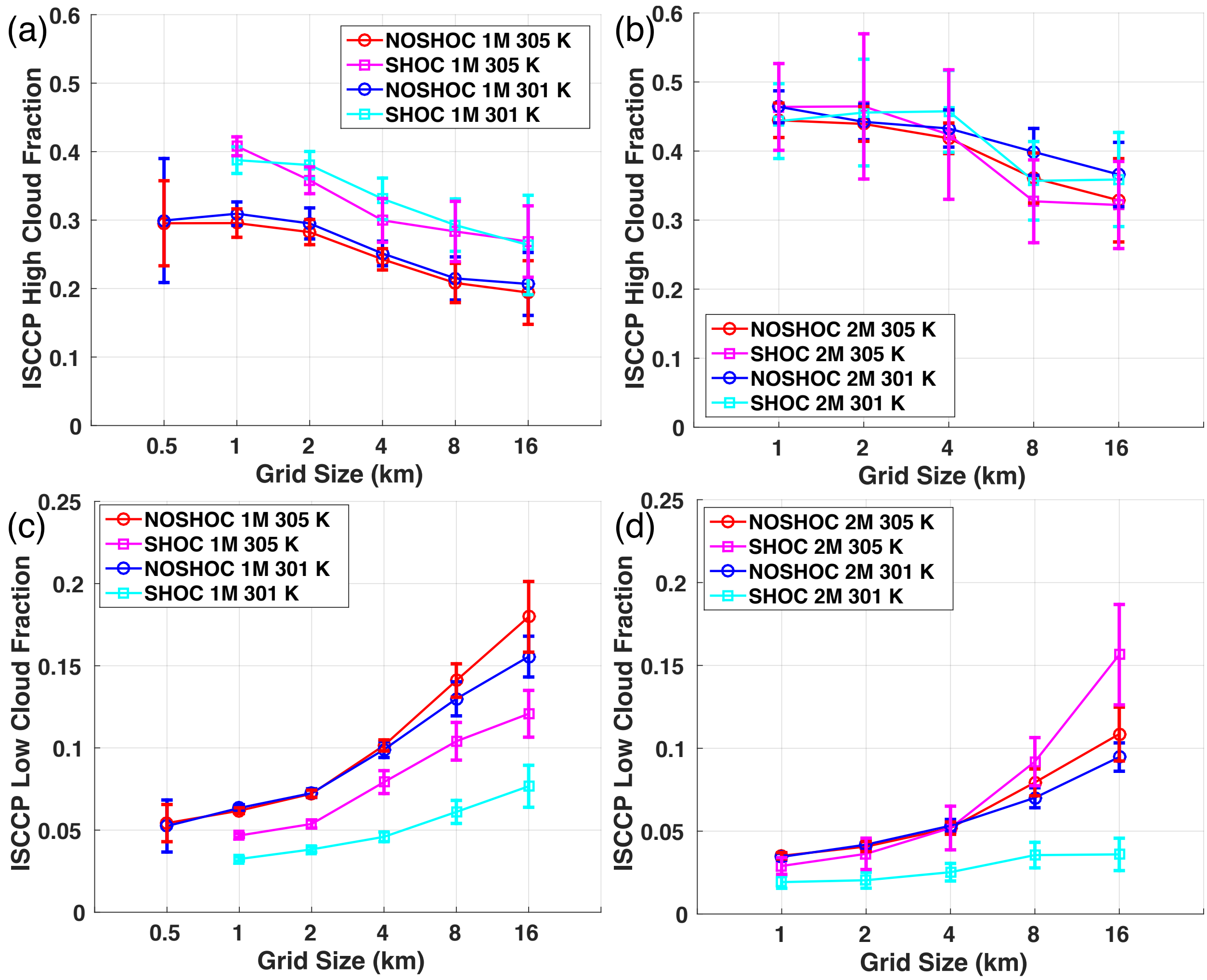

FIG. 2. RCE simulation 25-day averaged values of: a) ISCCP simulated high cloud fraction for single-moment microphysics runs, b) ISCCP simulated high cloud fraction for double-moment microphysics runs, c) ISCCP simulated low cloud fraction for single-moment microphysics runs, and d) ISCCP simulated low cloud fraction for double-moment microphysics runs. Each panel shows runs varying in grid size, SST, and turbulence parameterization scheme.

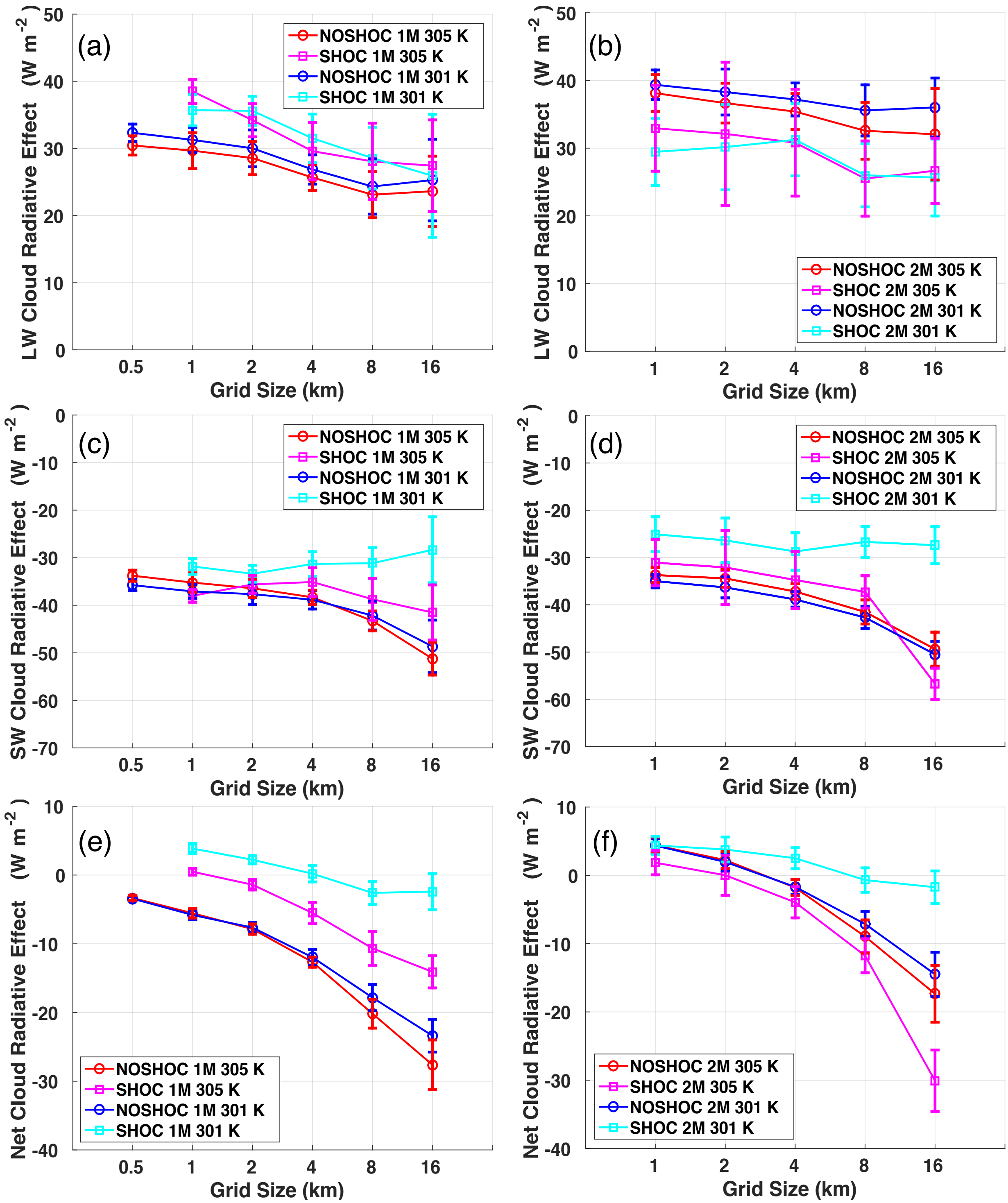

265 FIG. 3. RCE simulation 25-day averaged values of: a) LW cloud radiative effect for single-moment micro-
266 physics runs, b) LW cloud radiative effect for double-moment microphysics runs, c) SW cloud radiative effect
267 for single-moment microphysics runs, d) SW cloud radiative effect for double-moment microphysics runs, e) net
268 cloud radiative effect for single-moment microphysics runs, and f) net cloud radiative effect for double-moment
269 microphysics runs. Each panel shows runs varying in grid size, SST, and turbulence parameterization scheme.

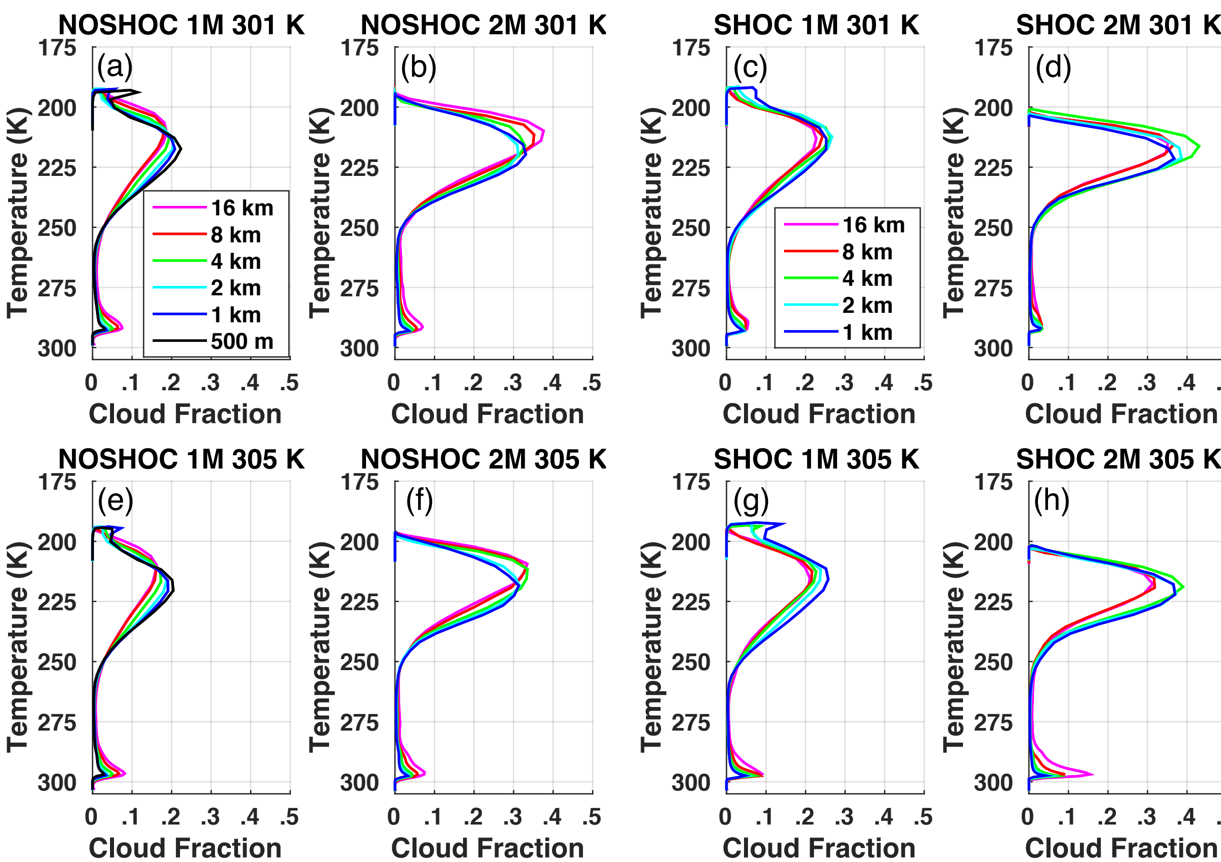

FIG. 4. RCE simulation 25-day averaged values of cloud fraction as a function of temperature. Panels separate runs based on 301 K SST (a,b,c,d) vs 305 K SST (e,f,g,h), NOSHOC (a,b,e,f) vs SHOC (c,d,g,h), and single-moment (a,c,e,g) vs double-moment (b,d,f,h) microphysics.

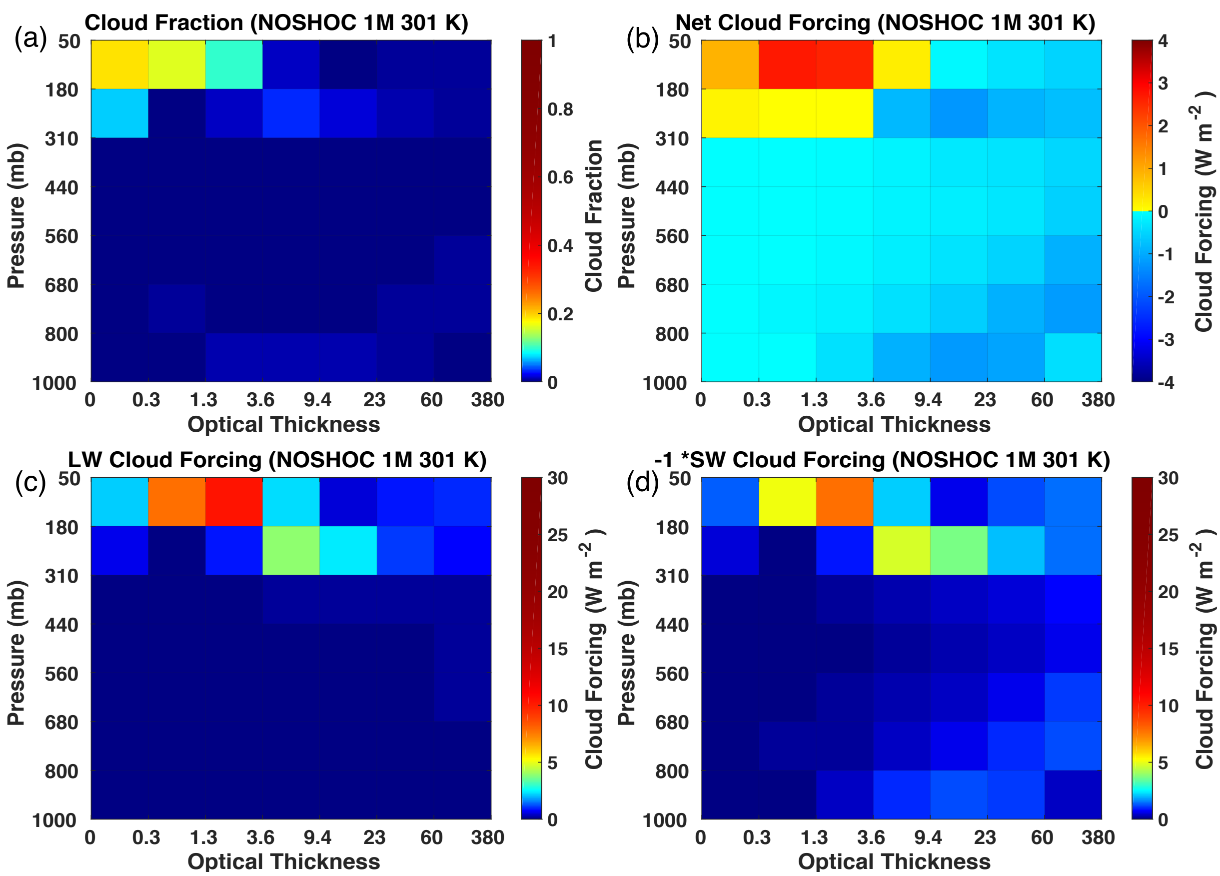

FIG. 5. RCE 25-day averaged 1-km single-moment NOSHOC 301K simulation cloud radiative kernel derived: a) cloud fraction, b) net cloud forcing, c) LW cloud forcing, and d) -1 * SW cloud forcing. Colorbars for a, c, and d are logarithmic.

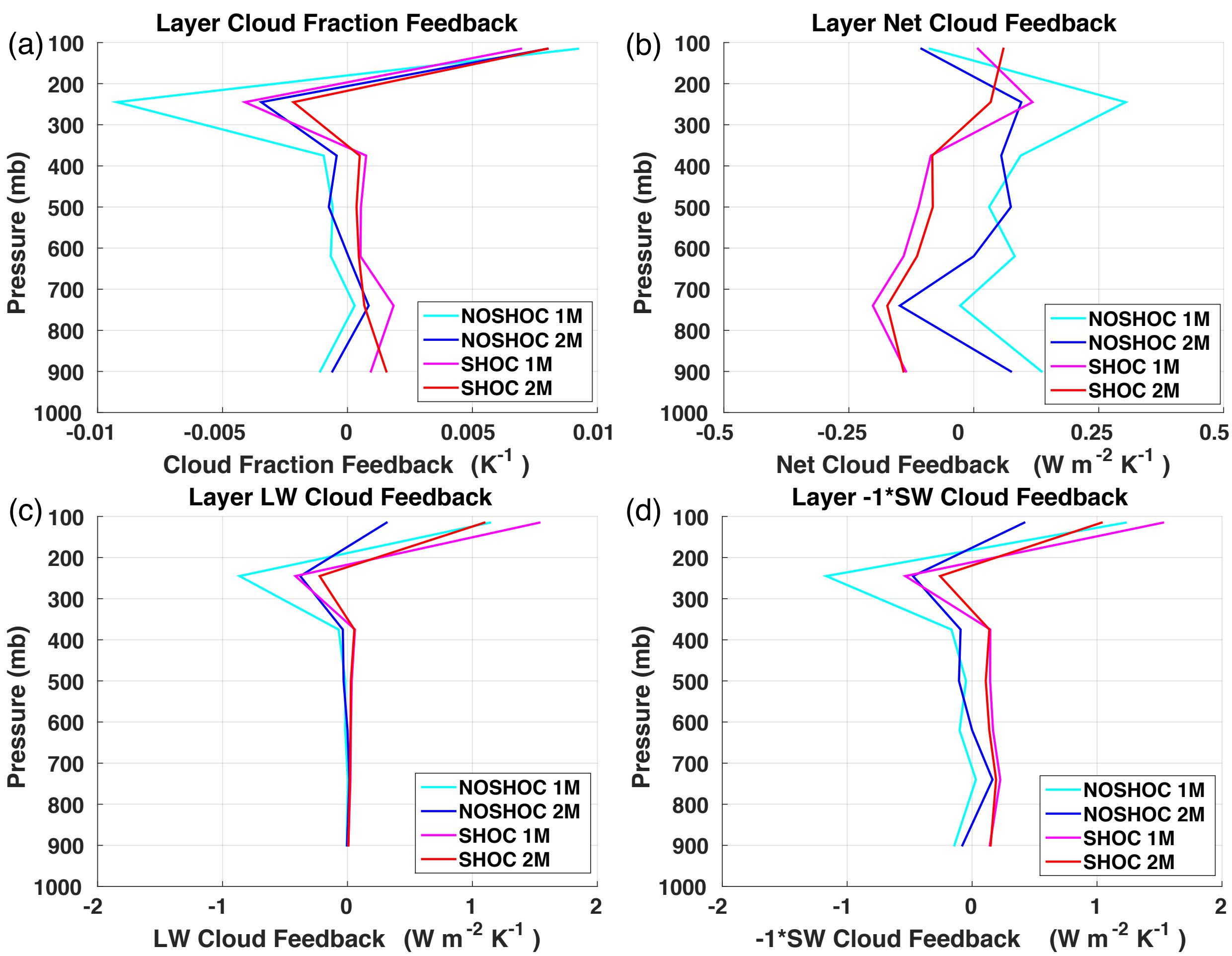

FIG. 6. Vertical profiles of 25-day averaged cloud radiative kernel derived: a) cloud fraction feedback, b) net cloud feedback, c) LW cloud feedback, and d) -1 * SW cloud feedback. Y-axis points are layer means of the pressures in Figure 9.